



The long-term corrosion behavior of FeCrAl(Si) alloys after breakaway oxidation at 600 °C

J. Eklund ^{*}, A. Persdotter, V. Ssenteza, T. Jonsson

Energy and Materials, Department of Chemistry and Chemical Engineering, Chalmers University of Technology, S-412 96 Göteborg, Sweden

ARTICLE INFO

Keywords:

FeCrAl
Silicon
SEM
EBSD
High temperature corrosion
Internal oxidation

ABSTRACT

The long-term corrosion behavior of three FeCrAl(Si) alloys has been investigated in two environments (K_2CO_3 and $KCl+H_2O$) at 600 °C. The FeCrAl alloy experienced breakaway oxidation in both environments but displayed a higher corrosion rate in $KCl+H_2O$. The FeCrAlSi alloys retained the primary protection in the presence of K_2CO_3 but underwent breakaway oxidation in the presence of $KCl+H_2O$. The FeCrAlSi alloys displayed considerably reduced corrosion rates, suggested to be an effect of the prevention of internal oxidation and the formation of non-continuous corundum-type oxide dispersed within the inward-growing scale.

1. Introduction

The phenomenon known as breakaway oxidation, which describes the sudden increase in oxidation rate upon breakdown of the protective oxide scale of steels containing Cr and/or Al, is a limiting factor in applications exhibiting harsh environments at high temperatures. The general conception of this event is that it marks the end of the lifetime of a metallic component. Thus, the majority of literature within the field of high temperature corrosion has been focused on preventing breakaway oxidation, either by improving the corrosion resistance of this protective oxide scale or by reducing the corrosivity of the present environment. However, under extremely harsh conditions, for example in the presence of alkali salts, the breakdown of the primarily protective oxide scale may not be prevented, and the lifetime of the component therefore depends on the corrosion behavior after breakaway oxidation.

Alkali salts (such as K_2CO_3 and KCl) and/or water vapor are commonly known to be highly corrosive at high temperatures. For example, both of these species are some of the main contributors to the extremely aggressive environment in biomass- and waste-fired boilers (especially the latter). A vast range of literature has been focused on understanding the corrosive effect of water vapor and KCl and how to mitigate the corrosion attack on metallic materials in the presence of these [1–31]. In the temperature range of the present study (around 600 °C), water vapor has been shown to deplete the Cr-rich scale of chromia-forming alloys through the formation of chromium-oxy-hydroxide, leading to the well-known phenomenon

chromium evaporation. KCl has been shown to degrade Cr-rich scales in a way similar to K_2CO_3 , reacting with the protective scale to form K_2CrO_4 . However, unlike K_2CO_3 , KCl contains Cl which has been shown to be corrosive on its own. The mechanism behind the Cl effect is not fully understood but a common explanation is that of the active oxidation mechanism [32,33] or the electrochemical adaptation of that approach [34].

Under these harsh conditions, ferritic steels, such as FeCr(Al) alloys, tend to form Fe-rich oxide in harsh environments (e.g. in the presence of alkali salts, such as K_2CO_3 or KCl) following breakaway oxidation. The Fe-rich oxide scale grows at a much higher rate than the Cr- and/or Al-rich corundum-type oxide scales and is therefore generally considered non-protective. However, recent studies on the behavior of FeCr(Al) alloys after breakaway oxidation have demonstrated the possibility of significantly reducing the growth rate of the Fe-rich oxide scale by adjusting the chemical composition of the alloys [2,35,36], which introduced the concepts of a primary (Cr- and/or Al-rich corundum-type oxide) and a secondary (Fe-rich oxide) protection. Persdotter et al. [36] and Eklund et al. [35] showed that FeCr(Al) alloys that had transitioned into the secondary corrosion regime, i.e. begun to form Fe-rich oxide, display almost identical corrosion behavior as pure iron and low-alloyed steels below a critical Cr content. However, upon exceeding this limit, a significant reduction in growth rate was observed. The critical Cr content was also shown to be reduced by the addition of Al (>18 wt% Cr for FeCrAl alloys and >25 wt% Cr for FeCr alloys). The reduced growth rate was attributed to the formation of a Cr-rich healing layer at the

* Corresponding author.

E-mail address: johekl@chalmers.se (J. Eklund).

metal/oxide interface. Thermodynamic calculations suggested that Cr and Al prevented internal oxidation through synergistic effects, which facilitated the formation of a healing layer. Eklund et al. [2] recently investigated the influence of Cr on the corrosion behavior of FeCrAlSi alloys in the presence of KCl which demonstrated that the incorporation of Si further reduced the critical Cr content (≥ 10 wt% Cr), necessary to form a slow-growing Fe-rich oxide scale (i.e. secondary protection). The positive effect of Si on the corrosion resistance of stainless steels and FeCrAl alloys has previously been reported in a wide range of literature and has been shown to improve both the primary and secondary protection of an alloy [11,37–47].

In previous studies on the behavior of FeCrAl alloys forming a good secondary protection, the exposure time durations have been relatively short, making it difficult to gage the applicability of this behavior in real applications where the necessary operating lifetime of the metallic components can be in the range of several years. The aim of the present study is to investigate the propagation behavior (long-term) of Fe-based alloys that has previously been shown to form a poor or a good secondary protection (fast- or slow-growing Fe-rich oxide respectively) in an attempt to unravel the mechanisms responsible for the differences in oxide growth rate. This was done by exposing three different FeCrAl(Si) alloys for 2000 h in the presence of K_2CO_3 and $KCl + H_2O(g)$ (separate exposures). A detailed microstructural investigation of the corrosion products was performed using SEM/EDX and EBSD. X-ray diffraction was used as a complement to the EBSD analysis for phase determination.

2. Experimental procedure

2.1. Sample preparation

In this study, three different FeCrAl(Si) model alloys (alloy compositions are shown in Table 1), were chosen based on their corrosion behavior in previous studies [2,39], in which Fe10CrAl formed fast-growing Fe-rich oxide while Fe15CrAlSi and Fe20CrAlSi formed slow-growing Fe-rich oxide. The model alloys were produced in the same way as described by Eklund et al. [2,39]. Prior to exposure, the sample coupons were ground with SiC paper (P500 to P4000) and polished with a diamond suspension (1 μm) to achieve a mirror-like finish.

2.2. Exposures

The initial weight of the samples was measured using a Mettler Toledo balance with microgram resolution. For samples to be exposed in the presence of KCl, the salt was deposited by spraying a water-ethanol (20:80) solution saturated with KCl. For samples to be exposed in the presence of K_2CO_3 , the salt was deposited by spraying a water-based solution saturated with K_2CO_3 . In both cases, the drying of the solutions on the sample surfaces was accelerated by simultaneously blowing warm air towards the sample. The procedure was repeated until an amount of 2 mg/cm^2 had been deposited on each sample. Redeposition of the salts at regular intervals during the exposures was not performed to make sure that thermal stresses were not induced in the oxide scales (risk of oxide scale spallation).

The alloys were exposed in tube furnaces in two different environments. In the presence of K_2CO_3 , a flow rate of 3 cm/s and a gas composition of 5% $O_2 + 95\% N_2$ (Bal.) was used. and in the presence of $KCl + H_2O(g)$, the gas flow consisted of 5% $O_2 + 20\% H_2O + N_2$ (Bal.). The flow rate was set to a lower value (0.1 cm/s) to reduce the evaporation rate of

KCl, thereby ensuring that the salt will remain on the sample surfaces during the entire exposure. This was motivated by previous observations, showing that KCl evaporate at a fast rate under the present exposure conditions [48]. To further reduce the evaporation rate of KCl, an KCl-filled alumina boat, was placed upstream of the samples to saturate the incoming gas with $KCl(g)$. The experimental set-up for the exposure in the presence of KCl and water vapor is explained in more detail by Ssenteza et al. [49]. Both exposures took place at a temperature of 600 °C and lasted for 2000 h. Samples were mounted vertically in alumina sample holders that were positioned in parallel to the gas flow. The mass gain of the samples, post-exposure, was recorded by weighing, using the same balance as before exposure.

2.3. Analysis

To enable microstructural analysis of the exposed samples, cross sections were prepared by dry cutting with a Leica EM TXP. To protect the corrosion products, thin Si-wafers were attached to one side of the samples surface prior to cutting. To allow for more detailed microstructural analysis, the cross sections were subsequently milled using a Gatan PECS II broad ion beam (BIB) instrument. The instrument was operated in planar polishing mode at 6, 4 and 2 kV for 1 h per voltage setting. Before BIB milling the cross sections were polished to a surface finish of 0.5 μm .

The composition and microstructure of the oxide scales were investigated with scanning electron microscopy (SEM) using an FEI Quanta 200 SEM equipped with an Oxford Instruments X-Max^N 80 T energy dispersive X-ray (EDX) detector (10–20 kV) as well as a Leo ULTRA 55 FEG SEM (2 kV). When presenting chemical compositions from the EDX analyses, oxygen will be excluded due to difficulties with accurately quantifying light elements.

EBSD analysis was performed using a Tescan Gaia3 equipped with a NordlysNano Camera (for EBSD analysis). The instrument was operated at 20 kV to obtain the Kikuchi patterns necessary for phase determination.

The inward-growing oxide scale was analyzed in further detail by means of Transmission electron microscopy (TEM), using an FEI Titan 80–300 TEM operated in conventional TEM mode at 300 keV. Focused ion beam (FIB) milling was used to prepare the TEM lamellae. The FIB-SEM instrument utilized was an FEI Versa3D LoVac DualBeam, which was operated in high vacuum mode at 30 keV, with varying beam currents (30 pA - 30 nA) throughout the lift-out procedure. To facilitate the localization of a representative region and ensuring that the lamellae contain the inward-growing oxide scale, the lift-out was performed on BIB-milled cross sections.

3. Results

3.1. Thermogravimetry

The three different model alloys investigated in this study was exposed for 2000 h in two different corrosive environments: in the presence of K_2CO_3 (5% $O_2 + 95\% N_2$) and in the presence of KCl and water vapor (5% $O_2 + 75\% N_2 + 20\% H_2O$). Fig. 1 shows the mass gain of the alloys after exposure and displays distinct differences in the two environments.

In the presence of K_2CO_3 , Fe10CrAl exhibited a high mass gain ($18.4 mg/cm^2$) which corresponds to a theoretical oxide thickness of 128 μm (based on the assumptions that the mass gain originates from the density change due to the ingress of oxygen and that only magnetite forms [50]). Meanwhile, both Fe15CrAlSi and Fe20CrAlSi exhibited very low mass gain (0.13 and 0.03 mg/cm^2 respectively) which corresponds to oxide thicknesses in the nanometer range, indicating that these alloys have resisted breakaway oxidation.

After exposure in the presence of KCl and water vapor, Fe10CrAl displayed an even higher mass gain ($35 mg/cm^2$), corresponding to a

Table 1
Nominal composition (wt%) of FeCrAl model alloys.

Alloy	Fe	Cr	Al	Si	Other elements
Fe10CrAl	Bal.	10	3	0	
Fe15CrAlSi	Bal.	15	3	2	C, N, Zr
Fe20CrAlSi	Bal.	20	3	2	

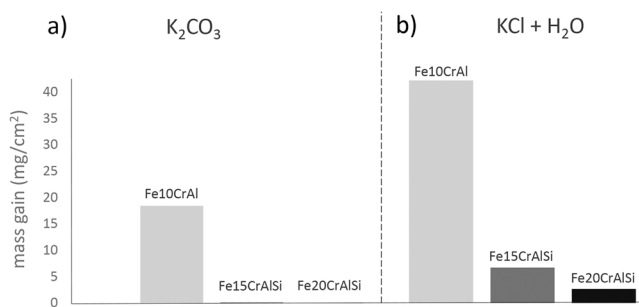


Fig. 1. Mass gains of the investigated alloys after exposure to a) $O_2 + N_2$ and K_2CO_3 and b) $O_2 + H_2O + N_2$ and KCl at 600 °C for 2000 h.

theoretical oxide thickness of 245 μm . Both Fe15CrAlSi and Fe20CrAlSi exhibited significantly lower mass gains than Fe10CrAl (5.6 mg/cm^2 and 2.2 mg/cm^2 respectively) corresponding to theoretical oxide

thicknesses of 39 μm and 15 μm respectively. However, in contrast to the exposure in the presence of K_2CO_3 , the high mass gains indicate that all alloys have experienced breakaway oxidation after exposure in the presence of KCl and water vapor.

3.2. Oxide microstructure

3.2.1. In the presence of K_2CO_3

As previously mentioned, the mass gain indicates that only the Fe10CrAl alloy experienced breakaway oxidation when exposed in the presence of K_2CO_3 . This was verified by the microstructural investigations. Thus, only the oxide formed on the Fe10CrAl alloy was investigated in detail.

The Fe10CrAl alloy formed a roughly 180 μm thick oxide scale, consisting of 110 μm thick outward-growing iron oxide and a 70 μm thick inward-growing (Fe, Cr, Al)-oxide, see Fig. 2a. Two layers could be distinguished by a difference in contrast in the outward-growing oxide

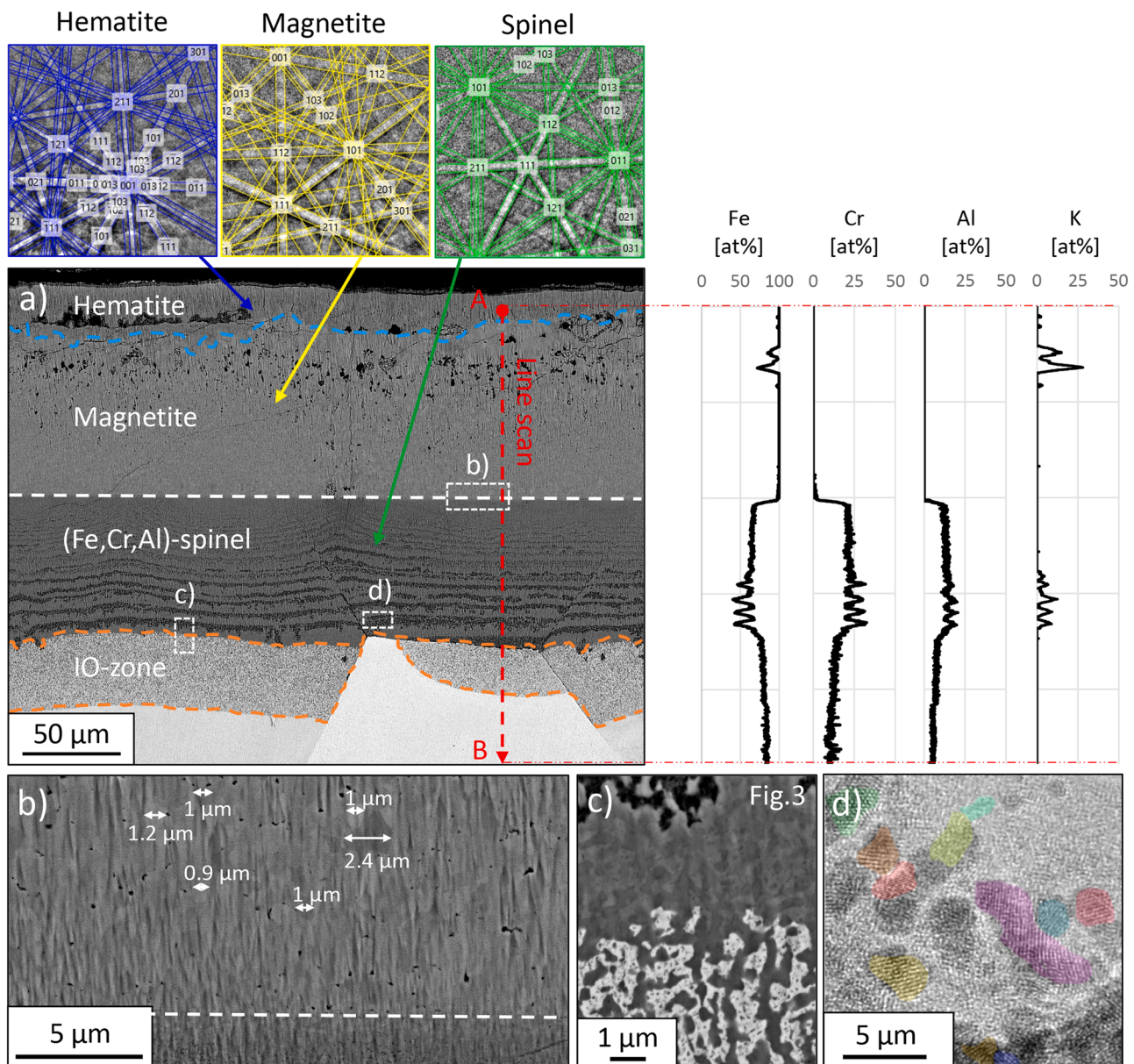


Fig. 2. SEM-BSE images of the Fe10CrAl alloy after exposure to $O_2 + N_2$ and K_2CO_3 at 600 °C for 2000 h. The Kikuchi patterns from the EBSD analysis confirms the presence of hematite, magnetite and mixed spinel. d) HR-TEM image of the nano-grains in the inward-growing spinel. Regions of different orientations are colored to better distinguish the size of the grains.

scale. EBSD analysis identified these layers as hematite (outer) and magnetite (inner), see inserted Kikuchi patterns in Fig. 2. The thickness of the hematite layer was ranging between 10 and 25 μm while the thickness of the magnetite layer was ranging between 80 and 95 μm . At closer examination, the magnetite layer was shown to have an average grain size of about 1 μm , see Fig. 2b. The grains of the hematite layer were difficult to distinguish because of their very fine-grained nature (usually in the range of 100–200 nm) but was shown to be in the range 250–1000 nm in diameter. Potassium was detected within the pores of the outward-growing oxide scale (see EDX-line scan in Fig. 2) and is interpreted as remnants of the deposited K_2CO_3 salt. The inward-growing scale was identified as a mixed spinel oxide through EBSD analysis (see Kikuchi pattern in Fig. 2) and consists of bright and dark contrast segments which alternates at a reducing frequency with oxide depth. The dark contrast segments originate from a porous microstructure, as shown in Fig. 2c. The EDX-analysis showed that the composition is relatively even throughout the inward-growing scale, consisting of ~15 at% Al, ~25 at% Cr and ~60 at% Fe (excluding oxygen). No significant enrichments of Cr could be observed close to the metal/oxide interface. Elevated potassium and chromium contents were found within the pores of the inward-growing scale. This is interpreted as K_2CrO_4 . Based on the position at which the K_2CrO_4 was detected, it is suggested to have been smeared over the cross section (from the oxide surface) during the preparation, and thereby ended up in the pores present in the inward-growing oxide scale. TEM analysis revealed a very fine-grained microstructure in the inward-growing scale with a grain size in the range of a few nm, see HR-TEM image in Fig. 2d. A roughly 40 μm thick internal oxidation zone has formed underneath the inward-growing oxide, consisting of oxidized and non-oxidized regions (see Fig. 2c). An inconsistency in the internal oxidation zone was observed in the proximity of a grain boundary at which no internal oxidation was observed. A few such examples were observed along the cross section (not shown). It is suggested that the higher rate of diffusion along the grain boundary may have locally increased the Cr concentration in these areas and inhibited the internal oxidation. This reasoning is further explained in the discussion section. Fig. 3 shows a magnified image of the interface between the oxide scale and the internal oxidation zone. The inner part of the inward-growing scale displays small alternating areas of different contrast with a microstructure similar to that of the internal oxidation zone (alternating areas of metal and oxide precipitates). No significant Cr-depletion was detected underneath the oxide scale.

3.2.2. In the presence of KCl and water vapor

The mass gain showed that all alloys displayed a transition into the

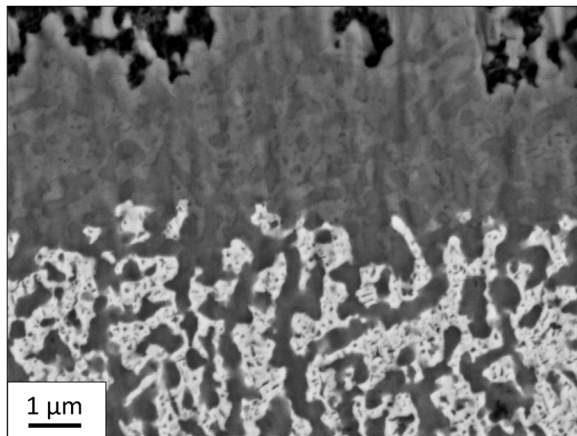


Fig. 3. Magnified SEM-BSE image of the interface between the oxide scale and the internal oxidation zone on the Fe10CrAl alloy after exposure to $\text{O}_2 + \text{N}_2$ and K_2CO_3 at 600 °C for 2000 h.

Table 2

Summary of oxide scale characteristics for the Fe10CrAl alloy after exposure in the presence of K_2CO_3 (5% O_2 + 95% N_2).

	Outward-growing oxide Hematite	Inward-growing oxide Magnetite	Total oxide thickness
Oxide thickness	10–25 μm	80–95 μm	70 μm
Grain size	0.25–1 μm	1 μm	A few nm 60 at% Fe 180 μm
Composition		25 at% Cr 15 at% Al	

secondary corrosion regime (breakaway oxidation) after exposure in the presence of KCl and water vapor. However, with the assumption that breakaway oxidation occurs within the first hour(s) (supported by previous research [2]), the thermogravimetric data suggests significant differences in corrosion behavior between the alloys within the secondary corrosion regime.

The Fe10CrAl alloy formed an oxide scale with a thickness of about 320 μm , see Fig. 4a. The scale consists of a roughly 180 μm thick outward-growing iron oxide and a 140 μm thick inward-growing (Fe, Cr, Al)-oxide. Two layers could be distinguished by the difference in contrast in the outward-growing scale. EBSD analysis identified the two layers as hematite (upper) and magnetite (bottom), see Kikuchi patterns in Fig. 4. The thickness of the hematite layer was relatively even around 80 μm while the magnetite layer had a thickness of about 95 μm . The magnetite layer was shown to be relatively coarse-grained with an average grain size of about 6 μm (ranging from 5 to 11 μm), see Fig. 4b. The grains of the hematite layer were shown to be more coarse-grained in comparison to what was observed for Fe10CrAl after exposure in the presence of K_2CO_3 with the grain size ranging from 1 to 2.5 μm . The inward-growing scale was identified as a mixed spinel oxide with EBSD analysis, see Kikuchi pattern in Fig. 4. At first glance, the contrast of the inward-growing scale seems relatively even. However, Fig. 4c shows that it contains small pores that are evenly distributed throughout the scale. The EDX line scan showed that the composition is even throughout the inward-growing scale, consisting of ~15 at% Al, ~25 at% Cr and ~60 at% Fe (excluding oxygen). Minor enrichments of Cr (35 at%) and Al (21%) could be observed close to the metal/oxide interface. However, this might be an effect of the higher density of pores in this area which could overestimate lighter elements, such as Al. TEM analysis revealed a very fine-grained microstructure in the inward-growing scale with a grain size in the range of a few nm, see HR-TEM image in Fig. 4d. A roughly 60 μm thick internal oxidation zone has formed underneath the inward-growing oxide. No significant Cr-depletion was detected underneath the oxide scale. No potassium or chlorides were found along the oxide scale.

The oxide scale formed by the Fe15CrAlSi alloy varies significantly in thickness over the surface, with the total thickness ranging from 10 to 50 μm . However, most of the surface is covered by a roughly 40 μm thick oxide scale, as shown in Fig. 5. The oxide scale consists of a 20–30 μm thick outward-growing iron oxide and a 10–18 μm thick inward-growing (Fe, Cr, Al, Si)-oxide scale. The outward-growing oxide scale consists of hematite (outer) and magnetite (inner) which was identified with EBSD analysis, see Kikuchi patterns in Fig. 5. While it is difficult to properly distinguish the different layers by contrast, the thickness of the hematite is about 8 μm while the thickness of the magnetite is about 14 μm (determined with EBSD). Naturally, these thicknesses vary depending on the total oxide thickness in a specific area. The grains of the hematite layer were fine-grained with a grain size in the range 140–400 nm. Magnetite was also relatively fine-grained with a grain size in the range 1–4 μm . The EDX line scan (shown in Fig. 5) displayed

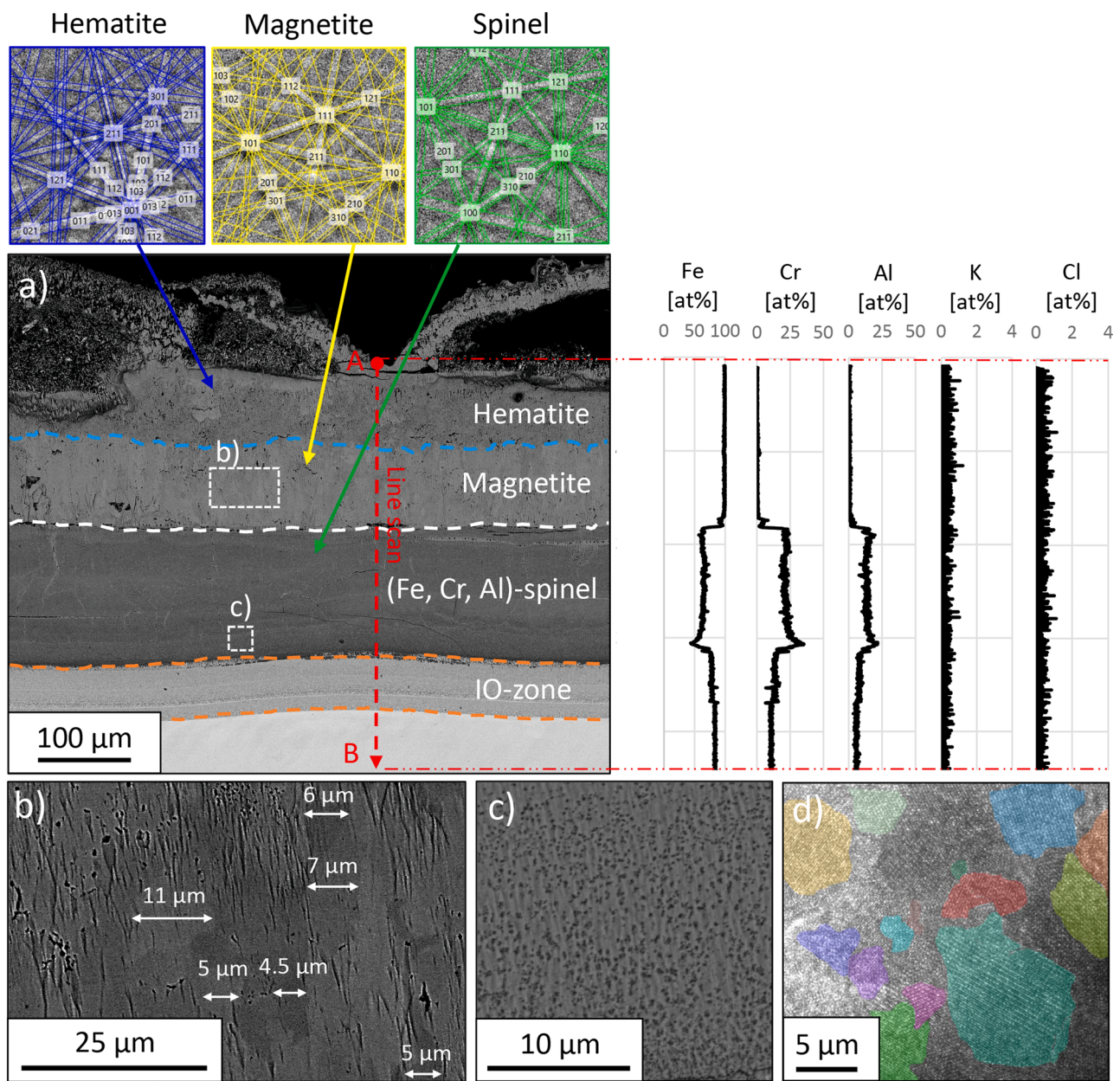


Fig. 4. SEM-BSE images of the Fe10CrAl alloy after exposure to $O_2 + H_2O + N_2$ and KCl at 600 °C for 2000 h. The Kikuchi patterns from the EBSD analysis confirms the presence of hematite, magnetite and mixed spinel. d) HR-TEM image of the nano-grains in the inward-growing spinel. Regions of different orientations are colored to better distinguish the size of the grains.

rather high compositional variations throughout the inward-growing scale. The segment of the inward-growing scale, closest to the outward/inward interface, is highly enriched in Cr (up to 75 at%) and contains nearly no Al or Si. Underneath this segment, the Cr concentration is reduced to about 15 at% while the Fe concentration goes up to about 50 at%. The concentration of Al fluctuates around 15 at% throughout the entire inward-growing scale (except close to the interface between inward-/outward-growing scale) while Si varies between 10 and 20 at%. The inner part of the inward-growing scale is highly enriched in Cr (up to 65 at%) with Fe concentrations as low as 10 at%. The Cr-rich segments are distinguished by the darker contrast in the SEM-BSE image (Fig. 5). The EDX analysis showed that Cr has been heavily depleted underneath the oxide scale to a depth of 4–15 μm (about 7 μm in the area of the line scan). EBSD analysis confirmed the presence of both a spinel crystal structure and a corundum-type crystal structure in the inward-growing scale. The phase variations seemed to occur from

grain to grain but the corundum-type crystal structure was found to a larger extent in the more Cr-enriched areas. A roughly 60 μm thick internal nitridation zone has formed underneath the inward-growing oxide (confirmed by nitrogen signal from EDX analysis). Minor remnants of KCl were found at the top of the oxide scale and close to the original metal surface. Additionally, small amounts of Cl were detected at the metal/oxide interface (up to 4 at%) which may be interpreted as the presence of metal chlorides as these tend to form at this interface where the pO_2 is low.

The Fe20CrAlSi alloy formed an oxide scale with a relatively even thickness (25–40 μm). The oxide scale shown in Fig. 6 consists of a 16–20 μm thick outward-growing iron oxide and a 9–13 μm thick inward-growing (Fe, Cr, Al, Si)-oxide scale. EBSD analysis confirmed the presence of both hematite (outer layer) and magnetite (inner layer) in the outward-growing scale. In similarity to the Fe15CrAlSi alloys, it is difficult to distinguish the border between the two layers, but the EBSD

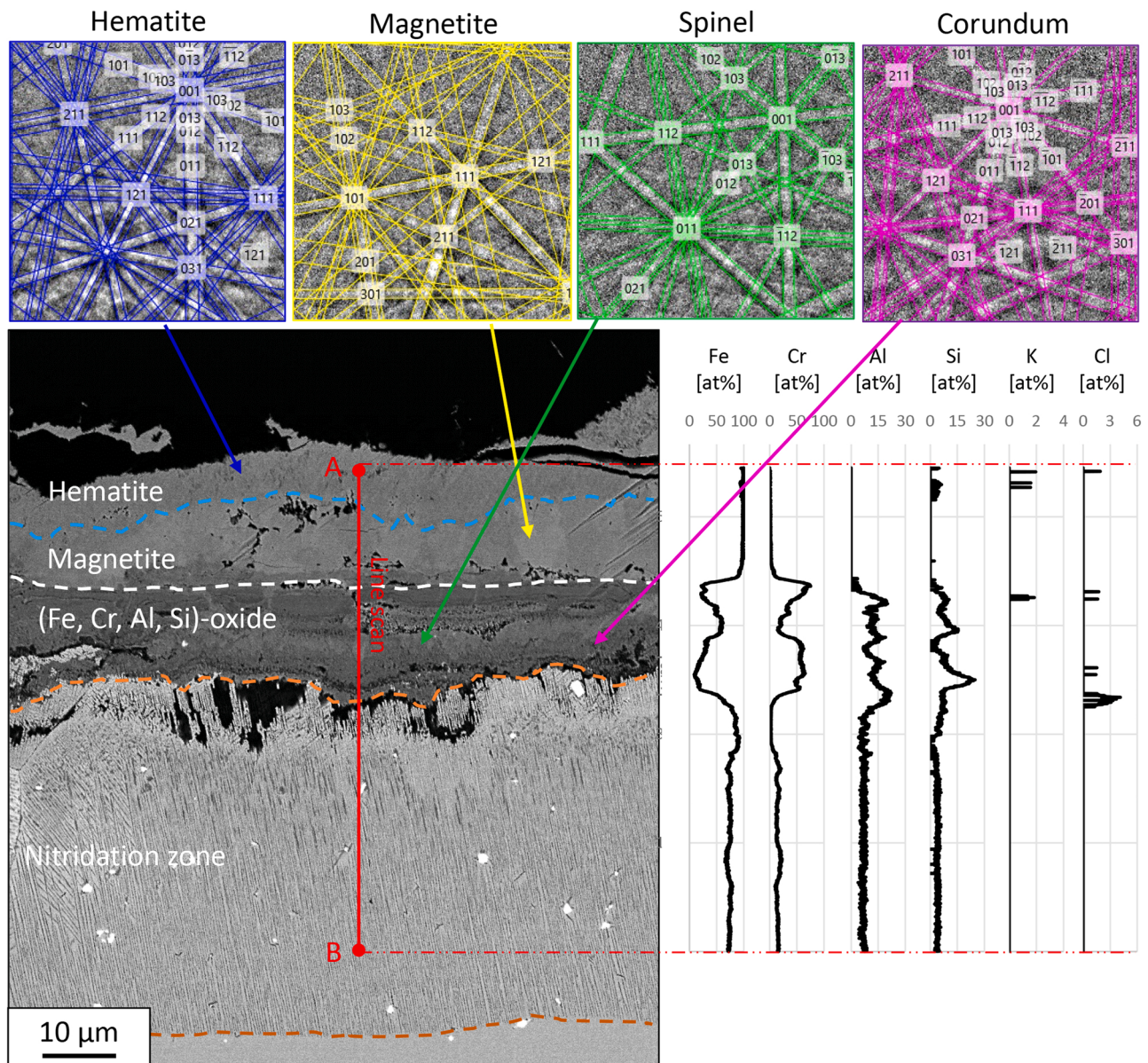


Fig. 5. SEM-BSE image of the Fe15CrAlSi alloy after exposure to $O_2 + H_2O + N_2$ and KCl at 600 °C for 2000 h. The Kikuchi patterns from the EBSD analysis confirms the presence of hematite, magnetite, mixed spinel and corundum-type oxide.

analysis indicates that the hematite thickness is about one third of the total thickness of the outward-growing oxide scale while the magnetite thickness is about two thirds. The EDX line scan (see Fig. 6) displayed a relatively even composition in the inward-growing scale. It also shows that the inward-growing scale is highly enriched in Cr (up to 75 at% Cr). Both the Al and Si contents remain fairly constant throughout the scale (ranging between 10 and 15 at%). Similar to the Fe15CrAlSi alloy, Cr has been heavily depleted underneath the oxide scale to a depth of about 6 μm. No remnants of KCl were detected but minor individual signals of K and Cl were detected within the outward-growing scale and inward-growing scale respectively. A roughly 60 μm thick internal nitridation zone has formed underneath the inward-growing oxide (confirmed by nitrogen signal from EDX analysis).

4. Discussion

It is well known that alkali salts, such as K_2CO_3 and KCl, and/or water vapor tend to cause breakaway oxidation for chromia-forming alloys at high temperatures (around 600 °C). The breakdown is

explained by the reaction between the salt and the initially formed Cr-rich corundum type oxide scale (the primary protection of the alloy) which results in Cr-depletion, either caused by the formation of K_2CrO_4 (K_2CO_3/KCl) or by the well-known phenomenon chromium evaporation (water vapor) [12,21,23,24,51].

In the present study, the long-term (2000 h) corrosion behavior of three FeCrAl(Si) model alloys have been investigated in two environments ($O_2 + N_2 + K_2CO_3$ and $O_2 + N_2 + H_2O + KCl$) known to cause breakaway oxidation [2,4–7,9–13,15,16,19,20,22,24,39,51–53]. The three alloys were selected based on previous research on their short-term corrosion behavior in similar environments [2,35,39]. However, in the present study, only one of the alloys (Fe10CrAl) experienced breakaway oxidation when exposed in the presence of K_2CO_3 , whereas all three alloys (Fe10CrAl, Fe15CrAlSi, Fe20CrAlSi) experienced breakaway in the presence of water vapor and KCl. Thus, in the upcoming sections the performance of the poorly protective Fe10CrAl will be discussed in relation to the more highly alloyed FeCrAlSi alloys (Fe15CrAlSi, Fe20CrAlSi). The microstructural evolution of the oxide scale formed on Fe10CrAl (poorly protective) exposed in the two

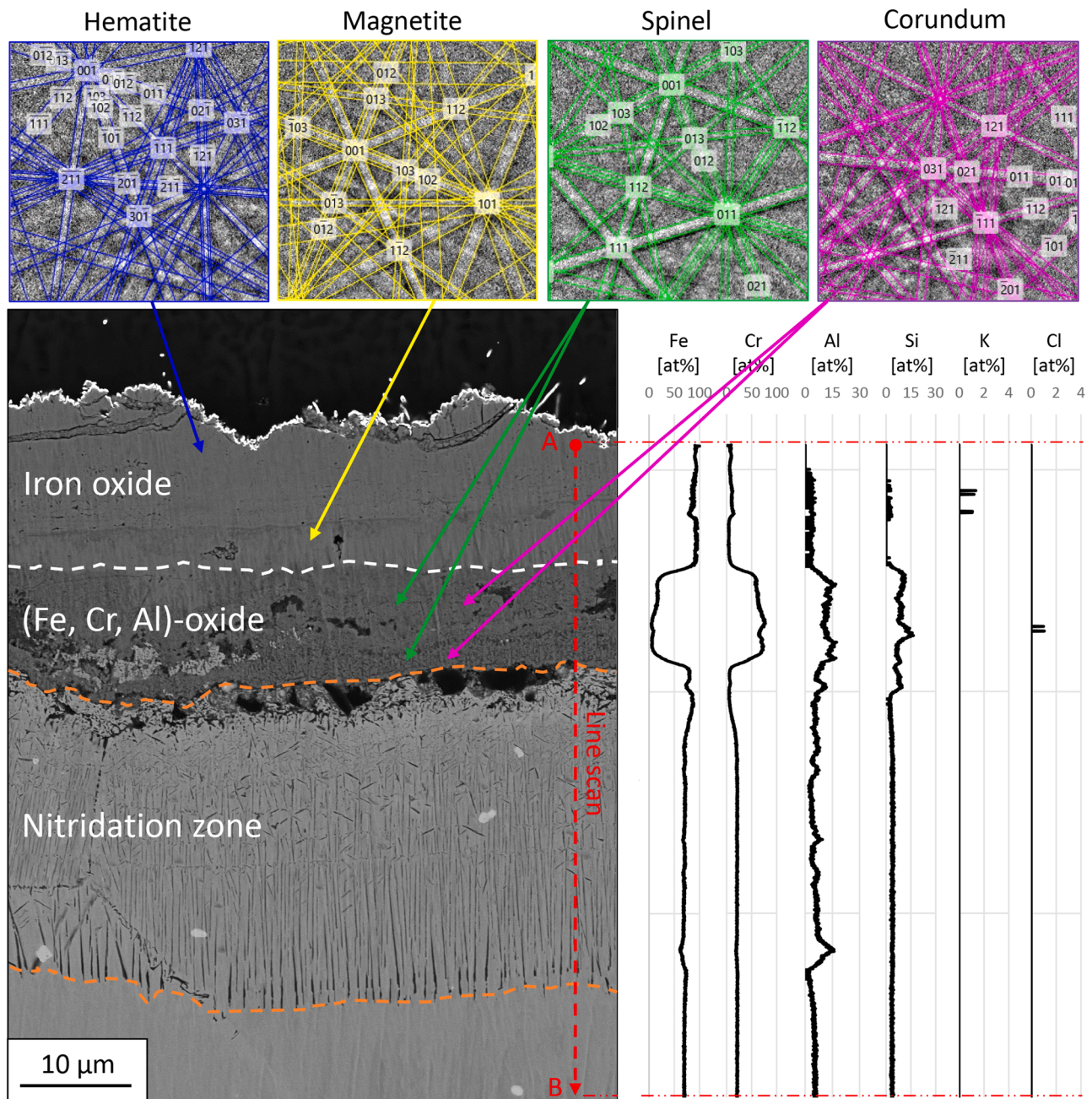


Fig. 6. SEM-BSE image of the Fe20CrAlSi alloy after exposure to $O_2 + H_2O + N_2$ and KCl at 600 °C for 2000 h. The Kikuchi patterns from the EBSD analysis confirms the presence of hematite, magnetite, mixed spinel and corundum-type oxide.

different environments is discussed in order to give insight into the growth mechanisms involved in the presence of water vapor and KCl following breakaway oxidation. Finally, the influence of alloying elements on the improved corrosion protection observed for the more highly alloyed FeCrAlSi alloys (Fe15CrAlSi, Fe20CrAlSi) is discussed.

4.1. Poor corrosion protection after breakaway – microstructural evolution in the presence (and absence) of water vapor and/or alkali salts

The presence of water vapor and KCl is generally understood to significantly increase the corrosion rate. This has especially been shown to be the case at lower temperature (400–500 °C) [3,54,55]. However, a study by Folkeson et al. indicated that the influence of KCl in the presence of water vapor on the growth rate of fast-growing iron-rich oxide scales became less significant with temperature (the accelerating effect

was not as prominent at 500 °C as at 400 °C) [3]. Eklund et al. showed that the Fe10Cr4Al alloy, (comparable to the Fe10CrAl exposed in this study), displayed almost identical oxide thickness after exposure in the presence and absence of KCl in a water vapor containing environment, indicating that KCl had no significant additional effect on the oxide growth kinetics of poorly protective iron-rich oxide scales (poor secondary protection) at 600 °C [39]. The observations that the effect of KCl on the oxide growth rate is reduced with increasing temperature indicate that the mechanism behind the KCl effect may be connected to grain boundary diffusion since the role of grain boundary diffusion in respect to the total diffusion (lattice diffusion + grain boundary diffusion) becomes less important with increasing temperature. Nevertheless, the microstructural evolution in the presence and absence of water vapor and KCl (i.e. difference in microstructure between the oxide scales formed in the two environments (K_2CO_3 versus water vapor/KCl) may

Table 3Summary of oxide scale characteristics for all alloys after exposure in the presence of KCl+H₂O.

	Outward-growing oxide		Inward-growing oxide	Total oxide thickness
Fe10CrAl	Hematite	Magnetite	Spinel	
Oxide thickness	80 µm	95 µm	140 µm	
Grain size	1–2.5 µm	6 (5–11) µm	A few nm 60 at% Fe 25 at% Cr 15 at% Al	320 µm
Composition				
Fe15CrAlSi	Hematite	Magnetite	Spinel + Corundum	
Oxide thickness	8 µm	14 µm	10–18 µm	
Grain size	0.14–0.4 µm	1–4 µm	-	40 µm
Composition			Outer [at%] Fe: 25 Cr: 75	
Fe20CrAlSi	Hematite	Magnetite	Mid [at%] Fe: 50 Cr: 15 Al: 15 Si: 10–20	
Oxide thickness	3–4 µm	6–9 µm	Inner [at%] Fe: 10–30 Cr: 50–65 Al: 15 Si: 10–20	
Grain size	0.15–0.4 µm	1–2.5 µm	Spinel + Corundum 9–13 µm	25–40 µm
Composition			5–25 at% Fe 50–75 at% Cr 10–15 at% Al 10–15 at% Si	

give important insights into the growth mechanism involved in the formation of the poorly protective multi-layered oxide scales.

The Fe10CrAl alloy exposed in the presence of K₂CO₃ formed a multi-layered Fe-rich oxide scale with a total scale thickness of 180 µm after 2000 h of exposure, whereas it formed a 70% thicker oxide scale (320 µm), in the presence of water vapor and KCl. Whether the increased corrosion rate is an effect of the water vapor, the chloride or a combined effect is difficult to determine (more than one variable is changing between the two environments).

The presence of water vapor has previously been shown to accelerate the growth rate of iron oxide [56–58]. Pujilaksono et al. showed that the oxidation rate of pure iron was increased in the presence of water vapor and that this was due to an increased growth rate of the hematite and magnetite layers while wüstite was unaffected [56]. Water vapor was suggested to influence the grain boundary transport in the hematite layer. Similar observations were observed for a low-alloyed steel (Fe2.25Cr) [58]. This is in good agreement with the present study which shows that a significantly thicker hematite layer formed in the presence of water vapor and KCl (~80 µm = 25% of the overall thickness), as compared to the Fe10CrAl alloy exposed to K₂CO₃ (~10–25 µm = 5–14% of the overall thickness). Hematite is generally considered a better diffusion barrier than magnetite (due to lower defect concentration) which should reduce the overall oxide growth rate. However, the hematite layer displays a highly porous microstructure after exposure to water vapor and KCl, which could negatively affect its efficiency as a diffusion barrier.

The oxide scale formed after 2000 h of exposure in the presence of K₂CO₃ consisted of 61% outward-growing and 39% inward-growing scale. This may be compared to the scale formed in exposure to water vapor and KCl, which consisted of 56% outward-growing iron oxide and 44% inward-growing scale. Thus, the ratio between outward- and inward-growing scale remained similar for the two exposure environments, however, with slightly more inward-growing scale in the presence of KCl/water vapor. This could be an indication of that the mechanism, known as active oxidation, which predicts a higher ratio of outward-growing scale due to the decomposition of metal chlorides into the respective oxide at higher pO₂, is not the main mechanism involved.

The oxide grain size is another factor that could have explained the increased growth rate in the presence of water vapor/KCl, since grain boundary diffusion is generally more rapid than bulk-diffusion. However, the average grain size of the magnetite layer was significantly larger after exposure to water vapor/KCl (~6 µm) as compared to K₂CO₃ (~1 µm) (see Fig. 2b and Fig. 3b), meaning that it contained less

grain boundaries for short-circuit diffusion. Thus, the magnetite grain size is does not seem to explain the difference in growth rate. The same applies to the grain size of the hematite layer in the two environment which was shown to be significantly larger in the presence of water vapor/KCl (see Tables 2 and 3).

The inward-growing scale formed on the Fe10CrAl alloy in the absence and presence of water vapor and KCl has almost identical chemical composition and the relative thickness of the inward-growing scales in the two different environments only differed slightly. However, the difference in microstructure of the inward-growing scale formed in the two environments is significant. The inward-growing scale formed on the Fe10CrAl alloy exposed in K₂CO₃ has a peculiar microstructure, consisting of dense and porous layers that alternate in a periodic manner with reducing frequency with increasing distance from the original metal surface. This microstructure could be observed already after short exposure durations (48 h) in previous studies [35,36], and the porous regions have been suggested to be remnants of internal oxidation [59] which is observed under these conditions. The internal oxidation zone has been shown to consist of an Fe-rich (Cr-depleted) alloy matrix surrounded by Cr-rich spinel precipitates [52,59] which is in good agreement with thermodynamic calculations (showing that the two-phase region BCC_{Fe} + S_{Cr} is stable underneath the inward-growing scale), see [35] and Fig. 7. During the initiation of internal oxidation, the alloy is attempting to form a continuous Cr-rich spinel layer. While failing to do so, due to lack of Cr, the alloy uses the Cr from the surrounding matrix to form the Cr-rich spinel precipitates, leaving the surrounding matrix heavily depleted in Cr, i.e., enriched in Fe. In the propagation of the oxidation process, it is reasonable to assume that the Fe-rich matrix in the internal oxidation zone is rapidly oxidized while the Cr-rich spinel precipitates remain fixed, resulting in the leaching of Fe and the formation of pores where the Fe-rich matrix once was. This is in good agreement with Fig. 2c which shows that the pores display a geometry almost identical to the Fe-rich matrix (bright contrast) in the internal oxidation zone.

The periodic nature of the alternations between dense and porous oxide segments is not fully understood. Eklund et al. [35] presented a hypothesis which was based on thermodynamics and the cross-over between the stability regions for pure spinel (S_{Cr}) and internal oxidation (BCC_{Fe} + S_{Cr}), caused by fluctuations in oxygen partial pressure, resulting in dense and porous regions alternating with the occurrence of internal oxidation. Hence, the internal oxidation itself was proposed to be discontinuous and of periodic nature. However, in this work, the microstructure of the dense segments of the inward-growing scale (see

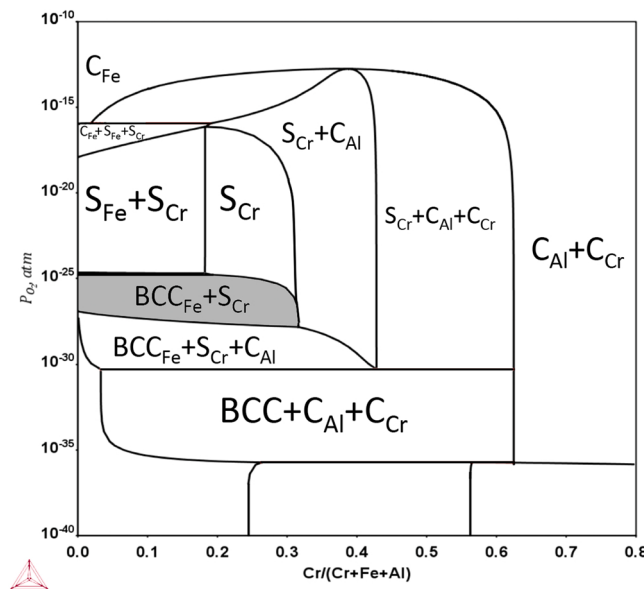


Fig. 7. Phase diagram for the FeCrAl system (Al content fixed at 15 at%) at 600 °C calculated with Thermo-Calc. The two-phase region marked in gray corresponds to the internal oxidation zone found underneath the oxide scale of the Fe10Cr3Al alloy.

Fig. 3), is observed to clearly resemble those of the oxide precipitates/Cr-depleted matrix in the internal oxidation zone, suggesting that the internal oxidation is active also in the formation of the dense layers. Thus, utilizing the new data and assuming that the internal oxidation is a continuous process that can be transformed into both dense and porous segments of inward-growing oxide, another mechanism must be responsible for the alternations.

As discussed above, it is reasonable to assume that the Cr-depleted, Fe-rich, matrix rapidly oxidizes as the corrosion front approaches, resulting in the leaching of Fe and formation of a porous segment of Cr-rich spinel. The process of forming the porous segment may give the underlying internally oxidized segment enough time to replenish the Cr-depleted, Fe-rich matrix with Cr which would enable the formation of a dense oxide segment. However, using Cr from the underlying matrix for the replenishment, would result in that the internally oxidized region below would not have enough Cr to replenish the Fe-rich matrix, leading to the formation of another porous segment. Thus, a periodic process has started, alternating between the leaching of Fe, forming porous segments, and Cr-replenishment of the internally oxidized region below, allowing for the formation of a dense oxide segment.

The frequency of the periodic alternations was observed to decrease as the process continued, resulting in thicker, porous and dense segments close to the metal/oxide interface. This may be explained by the process of leaching of Fe, and formation of pores, giving more time for the Cr-replenishment in the underlying internally oxidized region. The amount of Cr needed to replenish this segment would dictate the thickness of the Cr-depleted, Fe-rich matrix below, which would result in a subsequent thicker, porous segment. The leaching of Fe from the thicker porous segment would again give more time to replenish the Fe-rich matrix below, giving rise to the reduced frequency of the periodic alternations as observed. A schematic illustration of the suggested mechanism is shown in Fig. 8.

A few inconsistencies, in terms of discontinuity of the internal oxidation zone, was observed in Fig. 2. Since these inconsistencies seem to occur at grain boundaries, this is suggested to be an effect of the faster diffusion of Cr that may potentially be able to elevate the Cr content enough to inhibit the internal oxidation. Based on the slightly lower oxide thickness in this area, the inhibition has likely occurred recently. However, since similar observations have been made in previous studies

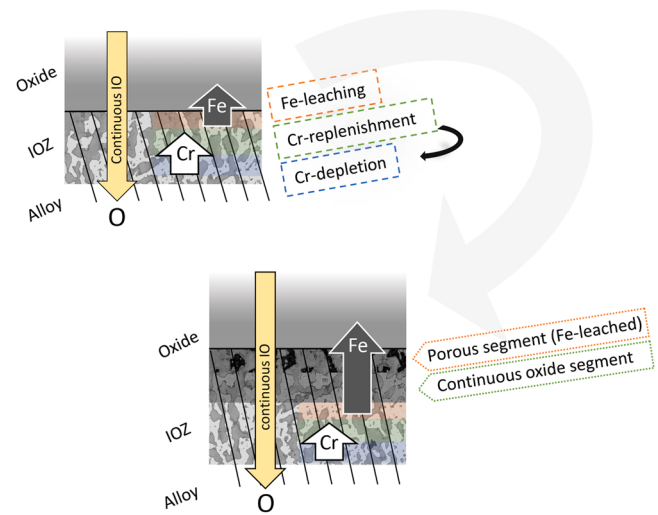


Fig. 8. Schematic illustration of the suggested mechanism for the formation of alternating dense and porous segments in the inward-growing scale. Internal oxidation results in the formation of Cr-rich spinel precipitates + Cr-depleted BCC in the internal oxidation zone (IOZ). The corrosion front is approaching the Cr-depleted matrix, which results in rapid leaching of iron, and consequently the formation of a porous, leached segment. The underlying region is given time to be replenished with Cr, allowing for the formation of Cr-rich spinel also around the Cr-rich spinel precipitates, resulting in a dense, continuous segment formed underneath the porous layer. The process continues periodically since the Cr-replenishment depletes the region underneath the dense segment (in Cr), hindering further Cr-replenishment, again resulting in rapid leaching of Fe and the formation of another porous segment.

after shorter exposures, this indicates that the inhibitions are temporary [39].

In similarity to the Fe10CrAl exposed in the presence of K₂CO₃, the oxide formed on Fe10CrAl when exposed to water vapor and KCl displays a porous structure in the inward-growing scale. However, the distribution of these pores differs significantly. Instead of dense and porous segments that alternate in a periodic manner (in the presence of K₂CO₃), the inward-growing oxide contains pores evenly distributed throughout the entire scale (water vapor and KCl). It is reasonable to assume that the absence of any dense segments in the scale further reduces the ability to act as a diffusion barrier which may explain the increased corrosion rate observed in the presence of water vapor and KCl. However, the mechanism behind the difference is not fully understood. Elaborating on the hypothesis regarding the origin of the alternating dense and porous bands, presented in the previous section, the ability to form the dense segments is dependent on that enough time is given to replenish the Fe-rich matrix in the internally oxidized region with Cr. It is reasonable to assume that any mechanisms that results in an increased oxide growth rate will increase the outward-diffusion of Fe ions (since the outward-growing oxide scale grows faster). If the leaching of Fe-ions during the formation of the porous oxide layer is too rapid, the Cr-diffusion within the alloy/internal oxidation zone may not be fast enough to replenish the Fe-rich matrix in the underlying internally oxidized region, thereby impeding the dense segments from forming, leading to the formation of a large porous segment throughout the entire inward-growing scale. Thus, it is suggested that the presence of water vapor and/or KCl increases the mobility of Fe-ions, which in turn would explain the accelerated oxide growth observed in the presence of these species.

Finally, it may be noted that the magnetite layer remains similar in thickness for the exposures in K₂CO₃ and KCl/H₂O(g). This indicates that the difference in thickness (i.e. growth rate) may be explained by the interplay between the outward growing hematite and the inward-growing spinel. In line with the hypothesis of pure Fe-leaching (from

the Cr-depleted metal in the internally oxidized zone) as explained above, a mass balance was performed for both exposure environments to investigate if the total amount of leached Fe from the IO-zone would add up to the increased amount of hematite observed. Thus, the mass balances were performed by the assumption that all Fe used for growing the hematite layer was taken from the estimated total volume of pores in the inward growing spinel (assumed to have formed as a result of Fe-leaching). The hematite (Fe_2O_3) layers were assumed to be dense for both exposure conditions, whereas the porosity of the inward-growing spinel was estimated from the microstructure observed in the SEM images. The porosity was estimated to be 16.5% of the total volume of the inward-growing spinel for the oxide formed on the sample exposed to K_2CO_3 (one third porous segments containing approximately 50% pores $\rightarrow (0.33 \times 0.5) \times 100 = 16.5\%$) and 25–30% for the sample exposed to KCl and water vapor. The mass balances added up for both samples ($m_{\text{Fe}}(\text{Fe}_2\text{O}_3) \approx m_{\text{Fe}}(\text{pores})$), strengthening the hypothesis that the porous microstructure is indeed a result of Fe-leaching and suggests that further oxidation of the poorly protective oxide can be explained solely by oxidation of pure Fe.

4.2. Influence of alloying elements on the improved corrosion protection

4.2.1. Improved primary protection - resistance to breakaway oxidation

While most chromia-forming alloys tend to experience breakaway oxidation in the presence of K_2CO_3 , the two more highly alloyed materials investigated in this paper, Fe15CrAlSi and Fe20CrAlSi, resisted breakaway oxidation. This was quite unexpected since FeCrAl alloys with similar composition (Fe18Cr3Al and Fe25Cr3Al) has been shown to transition into the secondary corrosion regime in this environment [35]. The main difference between these alloys is that the FeCrAl alloys in the present study contain Si. Minor additions of Si have been shown to benefit the corrosion resistance of FeCrAl alloys and stainless steels and its beneficial effects has become a topic of great interest [2,13,14,40–47, 60–66]. One of the most common explanations for improved corrosion resistance upon the addition of Si is that it enables the formation of a SiO_2 layer at the metal/oxide interface that acts as a diffusion barrier [38,40–43,46,62]. This is generally observed at higher temperatures ($>650^\circ\text{C}$) and in less aggressive environments (for example in the absence of alkali salts). Nevertheless, minor additions of Si have also been shown to greatly improve the primary protection of FeCrAl alloys (resisting breakaway oxidation in the presence of water vapor) at lower temperatures (600°C) when no SiO_2 layer could be observed [39,60, 67]. Asokan et al. showed that the chemical composition of the protective oxide scale (primary protection) significantly changed upon the addition of Si to the alloy [47]. In a dry environment, the Si-addition was shown to greatly increase the Al content in the protective oxide scale while reducing the Cr content, thereby making it less sensitive to the presence of water vapor. It was suggested that Si increased the activity of Al in the alloy while reducing the activity of Cr, which could also be done by increasing the Al content in the alloy. Persdotter et al. showed that a Fe18Cr6Al alloy was able to resist the transition from the primary to the secondary regime in the presence of K_2CO_3 [36]. As this is outside of the main focus of this work, the chemistry of the primary protective oxide scale was not investigated in the present study, however, the formation of a more Al-rich protective oxide scale (primary protection) could be an explanation to the resistance of Fe15CrAlSi and Fe20CrAlSi to break down in the presence of K_2CO_3 .

4.2.2. Improved secondary protection - the influence of Cr, Al and Si

As previously mentioned, all three alloys (Fe10CrAl, Fe15CrAlSi, Fe20CrAlSi) experienced breakaway in the presence of water vapor and KCl. While the more highly alloyed materials, Fe15CrAlSi and Fe20CrAlSi, do transition into the secondary corrosion regime in the presence of water vapor and KCl, the oxide growth rates of these are considerably lower than for Fe10CrAl. Exceeding a critical Cr content, and especially with the addition of Si, has previously been shown to

drastically reduce the corrosion rate of FeCrAl alloys after breakaway oxidation [2,35,60]. Microstructural investigations and thermodynamic calculations suggested that exceeding a critical Cr content prevents internal oxidation and promotes the formation of a Cr-rich healing layer while the presence of Al reduces the critical Cr content [35]. Minor additions of Si was also shown to significantly reduce the critical Cr content necessary to prevent internal oxidation [2]. While the mechanism behind this effect is not fully understood, a hypothesis was presented, suggesting that the Si^{4+} ions occupy tetrahedral sites in the mixed spinel, creating vacancies on other tetrahedral sites to maintain charge neutrality (knocking out Fe ions in the process) which in turns leads to a relative increase in Cr and Al concentration (since they occupy the octahedral sites and are not affected by the introduction of tetrahedral vacancies). In this study, both highly alloyed materials (Fe15CrAlSi, Fe20CrAlSi) displayed elevated Cr content in the inward-growing scale and neither suffered from internal oxidation.

In previous short-term (48 h) studies [2,35] several FeCrAl alloys (Fe18Cr3Al, Fe25Cr3Al and Fe15CrAlSi and Fe20CrAlSi), displaying a good secondary corrosion protection, were also found to form inward-growing scales that were highly enriched in Cr+Al. However, the phase of the inward-growing scale was not clearly determined. In the present study, both spinel and corundum-type crystal structures were identified in the inward-growing scale after 2000 h of exposure. Previous research usually reports that the formation of a corundum-type healing layer occurs close to the metal/oxide interface [65,68–72]. However, in the present study the EBSD analysis showed that the spinel and corundum phases co-existed throughout the inward-growing scale and that they seemingly could alternate from grain to grain. This is in agreement with thermodynamic calculations, which shows that Cr-rich spinel is in equilibrium with corundum-type oxide at higher Cr-concentrations, see Fig. 7. The phase transformations appeared to have occurred to a higher degree in areas with a high Cr concentration (found close to the metal/oxide interface) which should be expected due to the increased driving force in areas significantly exceeding the theoretical limit of trivalent ions in the spinel crystal structure (>67.7 cat%). Similar phase transformations were observed by Col et al. when exposing 304 L in O_2 at 850°C for 312 h. While the conditions significantly differs from the ones in the present study, similar partial phase transformations from spinel type oxide into chromia could be observed in Cr-enriched areas (close to the metal/oxide interface) [72]. The fact that the more highly alloyed materials form significantly slower-growing oxide scales within the secondary corrosion regime without necessarily forming a continuous layer, suggests that the reduced growth rate may not only be a result of the formation of a healing layer (or the general understanding of such a layer). This is further supported by the observations in previous studies [2,35] that show that the more highly alloyed materials display significantly reduced growth rates already within the first hours after breakaway oxidation, which is too early for a continuous healing layer to form at this temperature (600°C).

Internal nitridation zones were observed underneath the oxide scales on both Fe15CrAlSi and Fe20CrAlSi. This has previously been observed for FeCrAl alloys that forms a good secondary protection [2,4–7,35,36]. A reasonable question that arises is whether the nitridation will negatively affect the corrosion resistance of the alloy since the nitridation locks the aluminum in place in the form of aluminum nitrides. While nitridation may negatively affect the primary protection of FeCrAl alloys (less aluminum available to form alumina), the secondary protection is assumed to not be significantly affected by this factor. This is because the corrosion resistance within the secondary regime is not dependent on the formation of an alumina layer at the metal/oxide interface, which is further indicated in the present study. However, for scientific purposes, exposures should be performed in the absence of nitrogen to fully reveal the effect of nitridation on the secondary protection. It may in addition be noted that nitridation will change the microstructure of the alloy and thereby affect the mechanical properties. Nevertheless, while

this is an interesting phenomenon, it is outside of the scope of this investigation.

In summary, the present study demonstrates that the internal oxidation, and the rapid leaching of Fe as a result of this, is detrimental to the corrosion resistance within the secondary corrosion regime as it drastically increases the iron oxide growth rate. This suggests that preventing internal oxidation may be one of the most important factors in reducing the corrosion rate after breakaway oxidation. However, if internal oxidation may be prevented, the phase transformation from Cr-rich spinel to Cr-rich corundum-type oxide may play an increasingly important role in further decelerating the corrosion process. This study shows that this is not exclusively connected to the formation of a continuous healing layer. However, it is possible that the corundum phase in the inward-growing scale slows down the ion diffusion even though not forming a continuous layer. The mixed phase inward-growing scale would then act as a type of diffusion barrier for which the efficiency is dependent on the concentration of corundum-type oxide in the scale. This would explain the difference in growth rate between the Fe15CrAlSi and Fe20CrAlSi alloys since the inward-growing scale of the former contains less areas that are highly enriched in Cr, suggesting that it would contain a lower concentration of corundum-type oxide.

5. Conclusions

The long-term corrosion behavior within the propagation stage of the secondary corrosion has been investigated for alloys previously known to provide a poor or a good secondary protection (fast- or slow-growing iron-rich oxide scale) after breakaway oxidation at 600 °C. This was performed in two different oxidizing environments, in the presence of K₂CO₃ or H₂O+KCl, known to rapidly break down the primary protection, initiating breakaway oxidation.

In the presence of K₂CO₃, only the Fe10CrAl alloy (representing an alloy with a poor secondary protection) displayed breakaway oxidation. The ability of the Fe15CrAlSi and Fe20CrAlSi alloys (representing alloys with a good secondary protection) to retain the primary protection is suggested to be a result of the formation of a more Al-rich oxide scale (promoted by the minor additions of Si) which is able to withstand the Cr-depleting effect of K₂CO₃.

All investigated alloys transitioned into the secondary corrosion regime when exposed in the presence of water vapor and KCl. However, the two Si-containing alloys (Fe15CrAlSi, Fe20CrAlSi) displayed considerably lower oxide growth rates compared to the Fe10CrAl alloy. The main difference between the alloys forming a poor and good secondary corrosion protection is suggested to be the internal oxidation, observed underneath the poorly protective oxide scale, and the resulting microstructure of the inward-growing scale, which causes the growth rate to be exclusively determined by Fe-oxidation. Thus, the improved corrosion protection observed on the FeCrAlSi alloys is suggested to be an effect of the prevention of internal oxidation in combination with the formation of a non-continuous, Cr-rich, corundum-type oxide dispersed within the inward-growing scale.

In addition, the poorly protective scale formed on Fe10CrAl alloy exhibited significantly higher corrosion rate in the presence of water vapor and KCl compared to in the presence of K₂CO₃. The inward-growing scale was observed to be evenly porous in the presence of water vapor and KCl, whereas it formed a banded structure, with alternating porous and dense segments in the presence of K₂CO₃. The difference in porous microstructure is suggested to be caused by a more rapid Fe-leaching in the presence of water vapor and KCl as compared to K₂CO₃. More rapid Fe-leaching in combination with a more porous oxide scale would result in a higher oxide growth rate, which is in good agreement with the observations in this study.

CRediT authorship contribution statement

Johan Eklund: Conceptualization, Methodology, Validation,

Investigation, Data curation, Writing – original draft, Writing – review & editing, Visualization. **Amanda Persdotter:** Conceptualization, Investigation, Validation, Data curation, Writing – review & editing. **Vincent Ssenteza:** Methodology, Investigation, Writing – review & editing. **Torbjörn Jonsson:** Conceptualization, Writing – review & editing, Supervision, Project administration, Funding acquisition.

Declaration of Competing Interest

The authors declare that they have no known competing financial interests or personal relationships that could have appeared to influence the work reported in this paper.

Data availability

Data will be made available on request.

Acknowledgements

This work was carried out within the High Temperature Corrosion Centre (HTC) at Chalmers University of Technology. The authors are grateful to Kanthal AB for supporting and supplying materials for this study. The research was performed in part at the Chalmers Materials Analysis Laboratory, CMAL.

References

- [1] K.V. Dahl, A. Slomian, T.N. Lomholt, S. Kiamehr, F.B. Grumsen, M. Montgomery, T. Jonsson, Characterization of pack cemented Ni2Al3 coating exposed to KCl(s) induced corrosion at 600 °C, Mater. High. Temp. (2017) 1–8.
- [2] J. Eklund, I. Hanif, S. Bigdeli, T. Jonsson, High temperature corrosion behavior of FeCrAlSi model alloys in the presence of water vapor and KCl at 600 °C – The influence of Cr content, Corros. Sci. 198 (2022), 110114.
- [3] N. Folkeson, T. Jonsson, M. Halvarsson, L.G. Johansson, J.E. Svensson, The influence of small amounts of KCl(s) on the high temperature corrosion of a Fe-2.25Cr-1Mo steel at 400 and 500°C, Mater. Corr. 62 (2010) 606–615.
- [4] N. Israelsson, High temperature oxidation and chlorination of FeCrAl alloys, in, Chalmers University of Technology, Göteborg (2014).
- [5] N. Israelsson, J. Engkvist, K. Hellström, M. Halvarsson, J.-E. Svensson, L.-G. Johansson, KCl-Induced Corrosion of an FeCrAl Alloy at 600 °C in O₂ + H₂O Environment: The Effect of Pre-oxidation, Oxid. Met. 83 (2015) 29–53.
- [6] N. Israelsson, K. Hellström, J.-E. Svensson, L.-G. Johansson, KCl-Induced Corrosion of the FeCrAl Alloy Kanthal ® AF at 600 °C and the Effect of H₂O, Oxid. Met. 83 (2015) 1–27.
- [7] N. Israelsson, K.A. Unocic, K. Hellström, T. Jonsson, M. Norell, J.-E. Svensson, L.-G. Johansson, A. Microstructural, and Kinetic Investigation of the KCl-Induced Corrosion of an FeCrAl Alloy at 600 °C, Oxid. Met. 84 (2015) 105–127.
- [8] T. Jonsson, N. Folkeson, J.-E. Svensson, L.-G. Johansson, M.J.C.S. Halvarsson, An ESEM in situ investigation of initial stages of the KCl induced high temperature corrosion of a Fe-2.25 Cr-1Mo steel at 400C, 53, 2011; 2233–2246.
- [9] S. Karlsson, J. Pettersson, L.-G. Johansson, J.-E. Svensson, Alkali induced high temperature corrosion of stainless steel: the influence of NaCl, KCl and CaCl₂, Oxid. Met. 78 (2012) 83–102.
- [10] S. Kiamehr, K.V. Dahl, M. Montgomery, M.A.J. Somers, KCl-induced high temperature corrosion of selected commercial alloys, Mater. Corros. 67 (2015) 26–38.
- [11] S. Kiamehr, K.V. Dahl, M. Montgomery, M.A.J. Somers, KCl-induced high temperature corrosion of selected commercial alloys, Mater. Corros. 67 (2016) 26–38.
- [12] J. Lehmusto, P. Yrjas, B.J. Skrifvars, M. Hupa, High temperature corrosion of superheater steels by KCl and K₂CO₃ under dry and wet conditions, Fuel Process. Technol. 104 (2012) 253–264.
- [13] Y.S. Li, Y. Niu, M. Spiegel, High temperature interaction of Al/Si-modified Fe-Cr alloys with KCl, Corros. Sci. 49 (2007) 1799–1815.
- [14] Y.S. Li, M. Spiegel, S. Shimada, Effect of Al/Si addition on KCl induced corrosion of 9% Cr steel, Mater. Lett. 58 (2004) 3787–3791.
- [15] Y.C. Malede, K.V. Dahl, M. Montgomery, F.B. Grumsen, J. Hald, Effect of service exposure on KCl corrosion attack of AISI 347H FG steel, J. Mater. Sci. 54 (2019) 13787–13809.
- [16] Y.C. Malede, M. Montgomery, K.V. Dahl, J. Hald, Effect of microstructure on KCl corrosion attack of modified AISI 310 steel, Mater. High. Temp. 35 (2018) 243–254.
- [17] A. Persdotter, M. Sattari, E. Larsson, M.A. Olivas Ogaz, J. Liske, T. Jonsson, Oxidation of Fe-2.25Cr-1Mo in presence of KCl(s) at 400 °C – Crack formation and its influence on oxidation kinetics, Corros. Sci. 163 (2020), 108234.
- [18] C. Petterson, L.G. Johansson, J.E. Svensson, The Influence of Small Amounts of KCl(s) on the Initial Stages of the Corrosion of Alloy Sanicro 28 at 600 °C, Oxid. Met. 70 (2008) 241–256.

- [19] J. Pettersson, H. Asteman, J.E. Svensson, L.G. Johansson, KCl Induced Corrosion of a 304-type Austenitic Stainless Steel at 600°C; The Role of Potassium, *Oxid. Met.* 64 (2005) 23–41.
- [20] J. Pettersson, N. Folkeson, L.-G. Johansson, J.-E. Svensson, The Effects of KCl, K₂SO₄ and K₂CO₃ on the High Temperature Corrosion of a 304-Type Austenitic Stainless Steel, *Oxid. Met.* 76 (2011) 93–109.
- [21] J. Pettersson, J.E. Svensson, L.G. Johansson, Alkali Induced Corrosion of 304-type Austenitic Stainless Steel at 600 degrees C; Comparison between KCl, K₂CO₃ and K₂SO₄, in: P. Steinmetz, I.G. Wright, A. Galerie, D. Monceau, S. Mathieu (Eds.), *High Temperature Corrosion and Protection of Materials 7*, Pts 1 and 2, Trans Tech Publications Ltd, Durturn-Zurich, 2008, pp. 367–375.
- [22] J. Phother-Simon, T. Jonsson, J. Liske, Continuous KCl addition in high temperature exposures of 304 L – A way to mimic a boiler environment, *Corros. Sci.* 167 (2020) 8.
- [23] J. Sui, J. Lehmusto, M. Bergelin, L. Hupa, Initial oxidation mechanisms of stainless steel Sanicro 28 (35Fe27Cr31Ni) exposed to KCl, NaCl, and K₂CO₃ under dry and humid conditions at 535 °C, *Corros. Sci.* 155 (2019) 29–45.
- [24] J.X. Sui, J. Lehmusto, M. Bergelin, M. Hupa, The Effects of KCl, NaCl and K₂CO₃ on the High-Temperature Oxidation Onset of Sanicro 28 Steel, *Oxid. Met.* 85 (2016) 565–598.
- [25] E. Essuman, G.H. Meier, J. Zurek, M. Hänsel, L. Singheiser, W.J. Quadakkers, Enhanced internal oxidation as reason for breakdown of protective chromia scales on FeCr-alloys in water vapour containing gases, *Mater. Sci. Forum, Trans. Tech. Publ.* (2008) 699–706.
- [26] A. Galerie, Y. Wouters, M. Caillet, The Kinetic Behaviour of Metals in Water Vapour at High Temperatures: Can General Rules Be Proposed? *Mater. Sci. Forum*, 369–372 (2001) 231–238.
- [27] H. Götlind, F. Liu, J.E. Svensson, M. Halvarsson, L.G. Johansson, The Effect of Water Vapor on the Initial Stages of Oxidation of the FeCrAl Alloy Kanthal AF at 900 °C, *Oxid. Met.* 67 (2007) 251–266.
- [28] L. Liu, Z.-G. Yang, C. Zhang, M. Ueda, K. Kawamura, T. Maruyama, Effect of water vapour on the oxidation of Fe–13Cr–5Ni martensitic alloy at 973 K, *Corros. Sci.* 60 (2012) 90–97.
- [29] H. Asteman, K. Segerdahl, J.E. Svensson, L.G. Johansson, M. Halvarsson, J.E. Tang, p. trans tech, Oxidation of stainless steel in H₂O/O₂ environments - Role of chromium evaporation, in: P. Steinmetz, I.G. Wright, G. Meier, A. Galerie, B. Pieraggi, R. Podor (Eds.), *High Temperature Corrosion and Protection of Materials 6*, Pts 1 and 2, Proceedings, Trans Tech Publications Ltd, Zurich-Uetikon, 2004, pp. 775–782.
- [30] H. Asteman, J.E. Svensson, L.G. Johansson, Evidence for Chromium Evaporation Influencing the Oxidation of 304L: The Effect of Temperature and Flow Rate, *Oxid. Met.* 57 (2002) 193–216.
- [31] T. Sand, C. Geers, Y. Cao, J.E. Svensson, L.G. Johansson, Effective Reduction of Chromium-oxy-hydroxide Evaporation from Ni-Base Alloy 690, *Oxid. Met.* 92 (2019) 259–279.
- [32] J.-M. Abels, H.-H. Strehblow, A surface analytical approach to the high temperature chlorination behaviour of inconel 600 at 700C, *Corros. Sci.* 39 (1997) 115–132.
- [33] D. Bramhoff, H. Grabke, E. Reese, H. Schmidt, Einfluß von HCl und Cl₂ auf die Hochtemperaturkorrosion des 2 1/4 Cr 1 Mo-Stahls in Atmosphären mit hohen Sauerstoffdrücken, *Materials and Corrosion* 41 (1990) 303–307.
- [34] N. Folkeson, Chlorine Induced Corrosion in Biomass and Waste Fired Boilers: Laboratory and Field Investigations. Chalmers tekniska högskola. Department of Chemical Biological Engineering, Chalmers University of Technology., 2010.
- [35] J. Eklund, A. Persdotter, I. Hanif, S. Bigdeli, T. Jonsson, Secondary corrosion protection of FeCr(Al) model alloys at 600 °C – The influence of Cr and Al after breakaway corrosion, *Corros. Sci.* 189 (2021), 109584.
- [36] A. Persdotter, J. Eklund, J. Liske, T. Jonsson, Beyond Breakaway Corrosion - Influence of Chromium, Nickel and Aluminium on Corrosion of Iron-based Alloys at 600 °C, *Corros. Sci.* (2020), 108961.
- [37] S.N. Basu, G.J. Yurek, Effect of alloy grain size and silicon content on the oxidation of austenitic Fe-Cr-Ni-Mn-Si alloys in pure O₂, *Oxid. Met.* 36 (1991) 281–315.
- [38] J. Dunning, D. Alman, J.J.Oo.M. Rawers, Influence of silicon and aluminum additions on the oxidation resistance of a lean-chromium stainless steel, 57, 2002: 409–425.
- [39] J. Eklund, B. Jönsson, A. Persdotter, J. Liske, J.E. Svensson, T. Jonsson, The influence of silicon on the corrosion properties of FeCrAl model alloys in oxidizing environments at 600 °C, *Corros. Sci.* 144 (2018) 266–276.
- [40] L. Mikkelsen, S. Linderoth, J. Bilde-Sørensen, The effect of silicon addition on the high temperature oxidation of a Fe-Cr alloy, in: *Materials Science Forum, Trans Tech Publ.*, 2004, pp. 117–122.
- [41] T.D. Nguyen, J. Zhang, D.J. Young, Effects of Silicon on High Temperature Corrosion of Fe-Cr and Fe-Cr-Ni Alloys in Carbon Dioxide, *Oxid. Met.* 81 (2014) 549–574.
- [42] T.D. Nguyen, J. Zhang, D.J. Young, Effects of Silicon and Water Vapour on Corrosion of Fe-20Cr and Fe-20Cr-20Ni Alloys in CO₂ at 650 °C, *Oxid. Met.* 87 (2017) 541–573.
- [43] R. Pettersson, L. Liu, J.J.Ce Sund, science, technology, *Cycl. Oxid. Perform. Silicon-Alloy. Stainl. Steels Dry. moist air* 40 (2005) 211–216.
- [44] J.F. Radavich, Effect of silicon on high temperature oxidation of stainless steels, *CORROSION* 15 (1959) 73–77.
- [45] T. Sand, A. Edgren, C. Geers, V. Asokan, J. Eklund, T. Helander, J.E. Svensson, L. G. Johansson, Exploring the Effect of Silicon on the High Temperature Corrosion of Lean FeCrAl Alloys in Humid Air, *Oxid. Met.* 95 (2021) 221–238.
- [46] Y. Wouters, G. Bamba, A. Galerie, M. Mermoux, J.-P. Petit, Oxygen and Water Vapour Oxidation of 15Cr Ferritic Stainless Steels with Different Silicon Contents, *Mater. Sci. Forum*, 461–464 (2004) 839–848.
- [47] V. Asokan, J. Eklund, S. Bigdeli, T. Jonsson, The influence of Si on the primary protection of lean FeCrAl model alloys in O₂ and O₂+H₂O at 600 °C—A microstructural investigation, *Corros. Sci.* 179 (2021), 109155.
- [48] R.S. Bradley, P. Volans, Rates of Evaporation. VI. The Vapour Pressure and Rate of Evaporation of Potassium Chloride, *Proc. R. Soc. Lond. Ser. A, Math. Phys. Sci.* 217 (1953) 508–523.
- [49] V. Ssentza, J. Eklund, I. Hanif, J. Liske, T. Jonsson, High temperature corrosion resistance of FeCr(Ni, Al) alloys as bulk/overlay weld coatings in the presence of KCl at 600 °C, *Corros. Sci.* 213 (2023), 110896.
- [50] J. Eklund, High Temperature, Corrosion of FeCrAl Alloys in Biomass-And Waste-Fired Boilers-The Influence of Alloying Elements in Prediction and Mitigation of Corrosion in Harsh Environments, , Chalmers Tek. Hogskola (Swed.) (2020).
- [51] J. Lehmusto, B.J. Skrifvars, P. Yrjas, M. Hupa, Comparison of potassium chloride and potassium carbonate with respect to their tendency to cause high temperature corrosion of stainless 304L steel, *Fuel Process. Technol.* 105 (2013) 98–105.
- [52] T. Jonsson, S. Karlsson, H. Hooshyar, M. Sattari, J. Liske, J.E. Svensson, L. G. Johansson, Oxidation After Breakdown of the Chromium-Rich Scale on Stainless Steels at High Temperature: Internal Oxidation, *Oxid. Met.* 85 (2016) 509–536.
- [53] T. Jonsson, H. Larsson, S. Karlsson, H. Hooshyar, M. Sattari, J. Liske, J.E. Svensson, L.G. Johansson, High-Temperature Oxidation of FeCr(Ni) Alloys: The Behaviour After Breakaway, *Oxid. Met.* 87 (2017) 333–341.
- [54] M.A. Olivas-Ogaz, J. Eklund, A. Persdotter, M. Sattari, J. Liske, J.-E. Svensson, T. Jonsson, The Influence of Oxide-Scale Microstructure on KCl(s)-Induced Corrosion of Low-Alloyed Steel at 400 °C, *Oxid. Met.* 91 (2019) 291–310.
- [55] E. Larsson, J. Liske, A. Persdotter, T. Jonsson, J.E. Svensson, L.G. Johansson, The Influence of KCl and HCl on the High-Temperature Oxidation of a Fe-2.25Cr-1Mo Steel at 400 °C, *Oxid. Met.* 93 (2020) 29–52.
- [56] T. Jonsson, B. Pujilaksono, A. Fuchs, J.E. Svensson, L.G. Johansson, M. Halvarsson, The influence of H₂O on iron oxidation at 600C: a microstructural study, *Mater. Sci. Forum, Trans. Tech. Publ.* (2008) 1005–1012.
- [57] B. Pujilaksono, T. Jonsson, M. Halvarsson, J.-E. Svensson, L.-G. Johansson, Oxidation of iron at 400–600°C in dry and wet O₂, *Corros. Sci.* 52 (2010) 1560–1569.
- [58] B. Pujilaksono, T. Jonsson, H. Heidari, M. Halvarsson, J.E. Svensson, L. G. Johansson, Oxidation of Binary FeCr Alloys (Fe-2.25Cr, Fe-10Cr, Fe-18Cr and Fe-25Cr) in O₂ and in O₂ + H₂O Environment at 600 °C, *Oxid. Met.* 75 (2011) 183–207.
- [59] T. Jonsson, B. Pujilaksono, H. Heidari, F. Liu, J.E. Svensson, M. Halvarsson, L. G. Johansson, Oxidation of Fe-10Cr in O₂ and in O₂+H₂O environment at 600°C: A microstructural investigation, *Corros. Sci.* 75 (2013) 326–336.
- [60] J. Eklund, M.D. Paz, B. Jönsson, J. Liske, J.-E. Svensson, T. Jonsson, Field exposure of FeCrAl model alloys in a waste-fired boiler at 600°C: The influence of Cr and Si on the corrosion behaviour, 70, 2019: 1476–1485.
- [61] Y. Inoue, N. Hiraide, K. Ushioda, Effect of Si Addition on Oxidation Behavior of Nb containing Ferritic Stainless Steel, *Tetsu-to-Hagane, adypub*, 2016.
- [62] T. Jonsson, F. Liu, S. Canovic, H. Asteman, J.-E. Svensson, L.-G. Johansson, M. Halvarsson, Microstructural Investigation of the Effect of Water Vapour on the Oxidation of the Si-Containing FeCrNi Steel 353MA at 900 (Degree Sign) C in Oxygen, *Meet. Abstr. MA2006-02* (2006) 949.
- [63] H.-h Mao, X. Qi, J. Cao, L.-c An, Y.-t Yang, Effect of Si on high temperature oxidation of 30Cr13 stainless steel, *J. Iron Steel Res., Int.* 24 (2017) 561–568.
- [64] T. Oshima, Y. Habara, K. Kuroda, Effects of si on oxidation behaviors in Cr-Mn-Ni austenitic stainless steels, *Mater. Sci. Forum, Trans. Tech. Publ.* (2007) 4897–4902.
- [65] J. Robertson, M. Manning, Healing layer formation in Fe-Cr-Si ferritic steels, *Mater. Sci. Technol.* 5 (1989) 741–753.
- [66] F. Velasco, A. Bautista, A. González-Centeno, High-temperature oxidation and aqueous corrosion performance of ferritic, vacuum-sintered stainless steels prealloyed with Si, *Corros. Sci.* 51 (2009) 21–27.
- [67] V. Asokan, J. Eklund, T. Jonsson, The influence of Si on the primary protection of lean FeCrAl model alloys in O₂ and O₂+H₂O at 600 °C – A microstructural investigation, *Accept. Corros. Sci.* (2020).
- [68] T. Jonsson, S. Canovic, F. Liu, H. Asteman, J.E. Svensson, L.G. Johansson, M. Halvarsson, Microstructural investigation of the effect of water vapour on the oxidation of alloy 353 MA in oxygen at 700 and 900°C, *Mater. High. Temp.* 22 (2005) 231–243.
- [69] T. Gheno, D. Monceau, D.J. Young, Mechanism of breakaway oxidation of Fe-Cr and Fe-Cr-Ni alloys in dry and wet carbon dioxide, *Corros. Sci.* 64 (2012) 222–233.
- [70] T. Gheno, D. Monceau, D.J. Young, Kinetics of breakaway oxidation of Fe-Cr and Fe-Cr-Ni alloys in dry and wet carbon dioxide, *Corros. Sci.* 77 (2013) 246–256.
- [71] C. Pascal, V. Parry, E. Fedorova, M. Braccini, P. Chemelle, N. Meyer, D. Oquab, D. Monceau, Y. Wouters, M. Mantel, Breakaway oxidation of austenitic stainless steels induced by alloyed sulphur, *Corros. Sci.* 93 (2015) 100–108.
- [72] A. Col, V. Parry, C. Pascal, Oxidation of a Fe-18Cr-8Ni austenitic stainless steel at 850°C in O₂: Microstructure evolution during breakaway oxidation, *Corros. Sci.* 114 (2017) 17–27.